*Materials Science-Poland*, *Vol. 28*, *No. 2*, *2010*

# Synthesis of nano-$SnO_2$ and neural network simulation of its photocatalytic properties

A. E. KANDJANI, P. SALEHPOOR, M. F. TABRIZ*, N. A. AREFIAN, M. R. VAEZI

Materials and Energy Research Center (MERC), Karaj, Iran

Decolouration of Acid Red 27 (AR27) was investigated using UV irradiation in the presence of $SnO_2$ nanoparticles synthesized via the hydrothermal method. The average crystallite size of $SnO_2$ nanoparticles synthesized for 2 h was about 3.73 nm, according to X-ray analysis, and the specific surface area, which was estimated from the Halsey based *t* plot, was about 288 $m^2/g$. The effects of UV irradiation in the absence of a photocatalyst and in the presence of pure $SnO_2$ nanoparticles without any light source were negligible. An artificial neural network (ANN) was used to build an empirical model for the results. The results of neural network analysis are in good agreement with the experimental data which show that AR27 decolouration exhibits pseudo-first-order kinetic behaviour.

Keywords: *heterogeneous photocatalyst; advanced oxidation process; artificial neural network (ANN)*

## 1. Introduction

Dye wastewater has become one of the major by-products of several industries, especially the textile and paper industries. These hazardous materials introduce toxicity to their environments and water sources. Due to their simple dyeing procedure and good stability during washing processes, demands for the use of textile dyes are increasing drastically. Thus elaboration of procedures reducing harmful environmental effects of these dyes seems to be inevitable [1–3].

Many various methods of wastewater treatment have been applied, including: electroflotation, membrane filtration, electrocoagulation, ion exchange, irradiation, etc. [4]. Using solid catalysts, especially semiconductor photocatalysts, involves adsorption of pollutant molecules on a solid surface [5–7] and advanced oxidation processes (AOP). AOPs are the main processes involved in the photocatalytic decolouration of azo dyes. Oxide semiconductor photocatalysts are the most promising

*Corresponding author, email: Meisam.fa@gmail.com

semiconductors, which have been used successfully in the photocatalytic decolouration of azo dyes [8–12].

$SnO_2$ is a wide bandgap semiconductor, having the bandgap of about 3.65 eV at bulk state. $SnO_2$ has been reported as a suitable gas sensing oxide and recently its composites have been studied as promising semiconductors in the photocatalytic decolouration of wastewaters [13–17].

In the present paper, $SnO_2$ nanoparticles with small crystallite sizes and high specific surface area have been synthesised. Photocatalytic reactions involving these nanoparticles have been studied in detail, using Acid Red 27 as a pollutant. The results of experimental tests were analysed using artificial neural network (ANN) models. Also ANN has proved an important role for predicting a model based on the decolouration kinetics of AR27 by $SnO_2$ nanoparticles. To authors' best knowledge there are few papers which apply ANN in order to investigate decolouration kinetics in the presence of a heterogeneous photocatalysts [18–20].

## 2. Experimental

*Materials.* NaOH and $SnCl_4$ were purchased from Merck and were used without further purification. AR27 was purchased from Boyakh Saz Company (Iran). It is a commercial dye and was used without further purification. Its chemical structure and UV absorption spectra are shown in Fig. 1.

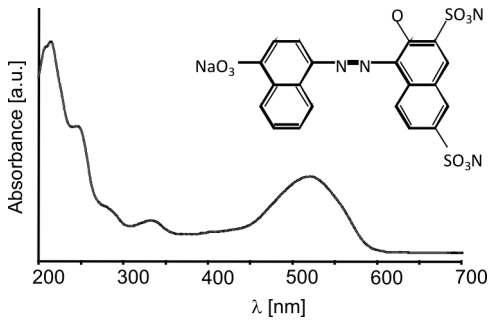


Fig. 1. The UV absorption spectrum and structure of AR27

*Method of synthesis*. The sample (SP-1) was prepared via the hydrothermal route. Firstly, 29.5 $cm^3$ of $SnCl_4$ was added dropwise to a 100 $cm^3$ of 1 M NaOH solution. The mixture was stirred continuously until a transparent solution formed. Then it was poured into a 35 $cm^3$ Teflon-lined autoclave and maintained at 170 °C for 2 h. After that, the autoclave was cooled to room temperature naturally and then the precipitates were filtered and washed several times with distilled water and ethanol. Finally, the obtained powder was dried at 50 °C for 24 h.

*Photocatalytic decolouration procedure*. All experiments were carried out in a 200 $cm^3$ batch photoreactor. The irradiation source was two mercury UV lamps

emitting light at 254 nm (15 W, UV-C, Philips, Holland) placed 15 cm above the bath photoreactor. In each experiment, 100 $cm^3$ of the dye solution with double the nominal concentration was prepared. Then, the photocatalyst powder was added to in 100 $cm^3$ of distilled water and sonicated for 30 min to achieve a homogeneous dispersion which was added to the dye solution to get the desired concentration. After very vigorous stirring, the mixture was left for 30 min to enable adsorption of AR27 on the surfaces of SnO2 powders in each reactor. The calculations of AR27 decolouration efficiency after the photochemical process were performed using the following formula:

$$X = \frac{C_0 - C}{C_0} \tag{1}$$

where $C_0$ and $C$ are the concentrations of the dye before and after irradiation, respectively.

*Analysis.* Crystallographic structures of the materials was studied using a Siemens D-5000 X-ray diffractometer (XRD) with $CuK_\alpha$ radiation ($\lambda$ = 0.154178 nm). Transmission electron microscope (Philips CM200) was used to study the morphologies of the prepared samples. The AR27 concentration was analyzed with a UV–Vis spectrophotometer (Aquarius-CECIL CE9500) at $\lambda$ = 521nm. It was used to monitor the decolouration of the dye and also to calculate the bandgap of the prepared $SnO_2$. The specific surface area of the nano-$SnO_2$ particles were determined by the Brunauer –Emmett–Teller and Halsey method (BET-$N_2$ adsorption, Micromeritics Gemini 2375). Also, the *t*-plot method was used to estimate the median pore size of the obtained sample. The powder was degassed at 200 °C in vacuum for 1.5 h before adsorption.

*Neural networks strategy.* In this study, our main goal was to identify an optimal ANN architecture. Due to the nonlinear behaviour of the input data, the architecture which produced the most accurate results was found to be a three-layer, feed-forward network. The first layer represents the input data which is fed into the system in a vector form. The hidden layer receives the results from the first layer and after processing, they are sent to third layer to be the desirable output for the system modelled with ANN. Figure 2 shows the scheme of this architecture. The activation functions were considered to be linear for the first and third layers

$$U_i = \sum_{j=1}^{n} W_{ij} X_j \tag{2}$$

A linear activation function was not the best type to be used in the second layer, and after testing various activation functions, the logarithmic sigmoid was found to be the best type to deliver the desired results [21]

$$F\left(U_i = \frac{1}{1+e^{-U_i}}\right) \tag{3}$$

For the sake of simplicity, the training algorithm used for the ANN was a basic back propagation algorithm implemented in C++. This algorithm enabled one to achieve the best possible result, with the accuracy of about $10^{-4}$. By using this algorithm, errors will decrease to reach a reasonable range by changing weights to reflect errors.

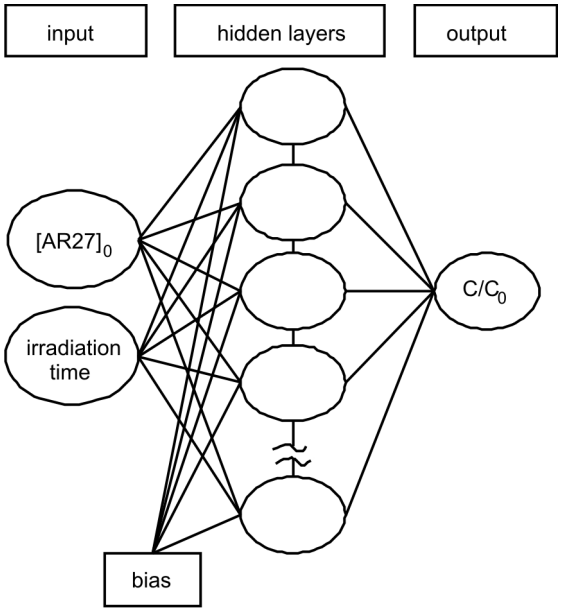


Fig. 2. Architecture of a feed-forward neural network with three layers and two inputs for decolouration analysis

Figure 3 shows the effect of number of neurons in the hidden layer on the overall performance of the neural network.

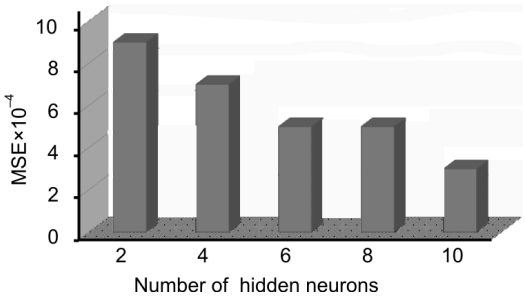


Fig. 3. Effect of number of neurons in the hidden layer on the overall performance of the neural network

# 3. Results and discussion

## 3.1. Synthesis

X-Ray diffraction patterns of samples are shown in Fig. 4. The Bragg peaks in all samples are in good agreement with those of cassiterite $SnO_2$ having a rutile structure (space group $p42/mnm$) with $a = 4.73727$ Å and $c = 3.186383$ Å.

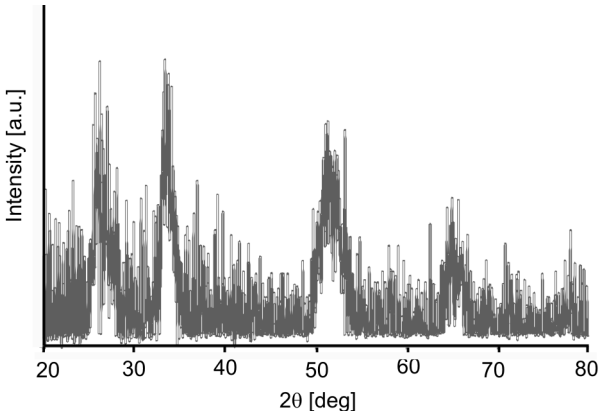


Fig. 4. XRD Pattern of SP-1

The average crystallite sizes were calculated from the full width at half maximum (FWHM) of the diffraction peaks of (101) planes using the Debbye–Scherrer formula:

$$D = \frac{k\lambda}{\beta \cos\theta} \tag{4}$$

where $D$ is the mean crystallite size, $k$ is a grain shape dependent constant (assumed to be 0.89), $\lambda$ is the wavelength of the incident beam, $\theta$ is the Bragg reflection peak and $\beta$ is the full width at half maximum [22]. The obtained results are listed in Table 1.

Table 1. The properties of SP-1 sample

| Average crystallite-size [nm] | Specific surface area [$m^2/g$] | Initial absorbance of AR27 after 30min |
|---|---|---|
| 3.73±0.05 | 188 | 0.071 |

In Figure 5, TEM images of SP-1 sample are shown. Under low magnification (Fig. 5a), it can be seen that the grid was covered by thin layers of $SnO_2$, also some agglomerates with median sizes of about 300 nm are visible. The selected area electron diffraction pattern (SAED) taken from these fine particles is shown in Fig. 5b.

The four indicated diffusion rings were identified as diffractions from the (211), (310), (312) and (411) planes of rutile type $SnO_2$. These types of diffused rings are attributed to extremely fine grain structures. A higher magnification image (Fig. 5b) shows that these layers and agglomerates are composed of fine spherical particles, typically having diameters smaller than 5 nm. Due to the extremely fine particles and strong agglomeration tendency in these samples, estimation of the true particle size distribution would involve high statistical errors. Therefore the median size of particles has not been indicated here.

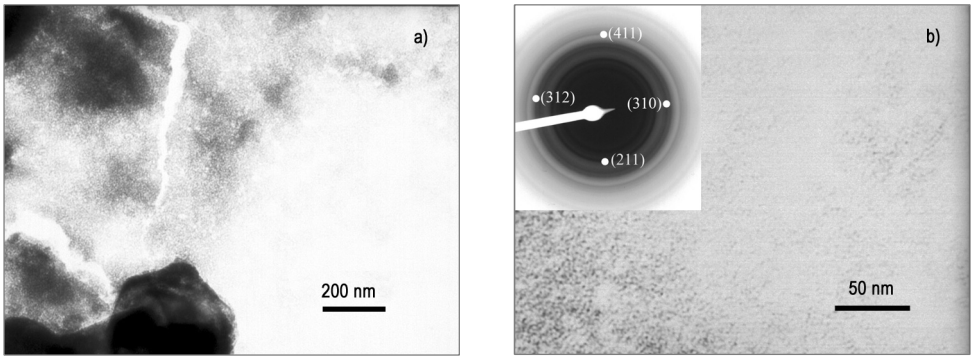


Fig. 5. TEM Images of SP-1

The direct bandgap values of the $SnO_2$ nanoparticles were estimated using UV absorption spectra. Figure 6 shows the UV-Vis absorption data. The sample shows a blue shift in comparison with its bulk state. Such a shift in the onset of absorption indicates a decreasing optical bandgap of the semiconductor, which is attributed to size quantization effects. The bandgap of the prepared sample was estimated to be ca. 4.15 eV.

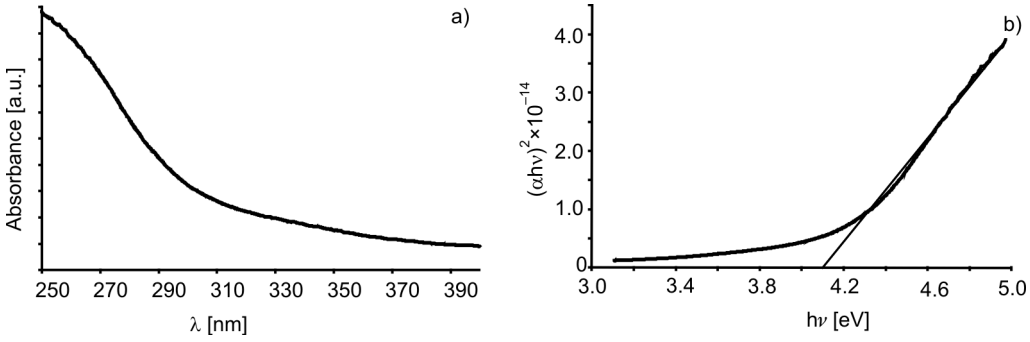


Fig. 6. UV absorption spectrum (a) and bandgap of the prepared $SnO_2$

The specific surface areas of the obtained samples were calculated from the Brunauer–Emmett–Teller (BET) equation. The obtained results are listed in Table 1. The high

surface area of these samples makes them good candidates as absorbents. Adsorption isotherms of the sample correlate strongly with a type I isotherm, as shown in Fig. 7a.

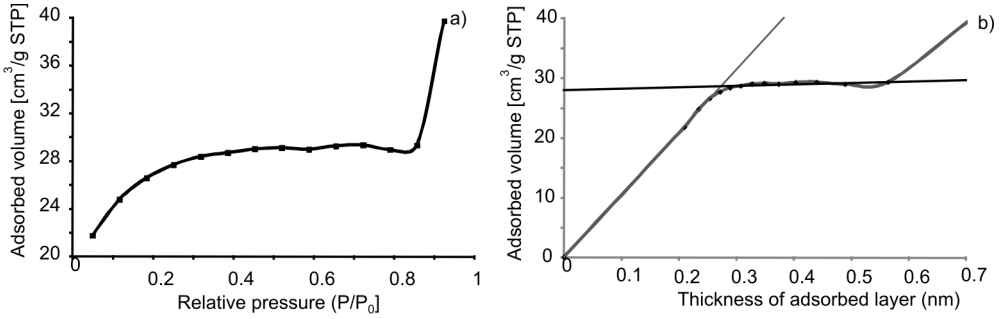


Fig. 7. BET adsorption isotherm (a) and t-plot of the sample (b)

It has been shown that if a solid contains micropores, its adsorption isotherm tends to resemble a type I isotherm. This phenomenon is attributable to overlapping of potential fields of neighbouring walls of porosities and corresponding by the increase in interaction energy of solid with gas molecules [23, 24].

The Halsey equation is generally used as estimation for the statistical thickness of adsorbed film as a function of nitrogen adsorption pressure at 77 K (the *t*-method) [25]

$$t = 0.354\left(\frac{5}{\ln\frac{P_0}{P}}\right)^{1/3} \quad [\text{nm}] \tag{5}$$

It can be used for calculating the monolayer surface area and the micropore volume size of the powders, as shown in Fig. 7b. The results are listed in Table 2.

Table 2. Results of the *t*-method for surface area and micropore volume of the SP-1 sample

| Slope 1 [$cm^3$ STP/(g·nm)] | Slope 2 [$cm^3$ STP/(g·nm)] | Intercept [$cm^3$ STP/g] | Total area [$m^2$/g] | External area [$m^2$/g] | Micropore volume [$cm^3$/g] |
|---|---|---|---|---|---|
| 187.4780 | 2.5968 | 47.0607 | 288.9462 | 4.0023 | 0.0729 |

This type of adsorption can be observed in many solids like xerogel of silica [26], titania [27] and zeolites [28]. Due to the fine particle sizes of these samples and their high agglomeration tendency, the resultant agglomerates act as microporous hosts.

During the hydrothermal process each mole of $Sn^{4+}$ ions react with 4 moles of $OH^-$ ions to form crystals [29]:

$$Sn^{4+} + 4OH^- \longrightarrow Sn(OH)_4 + 4H^+ \tag{6}$$

$$Sn(OH)_4 \longrightarrow SnO_2 + H_2O \tag{7}$$

Formation of crystalline $SnO_2$ during the hydrothermal process can be described using the growth unit model, first proposed by Zhong [30]. It is assumed in the model that during the crystallization process cations are in the form of complexes with $OH^-$ ions as ligands. The growth units are complexes whose coordination numbers are the same as those of the crystal. It has been shown that during the hydrothermal formation of $SnO_2$, the growth units are complexes of $Sn(OH)_6^{2-}$ [31, 32].

### 3.2. Experimental data for decolouration of AR27

Figure 8 Shows the UV-Vis spectra of AR27 dissolved in water with SP-1 colloidal nanoparticles.

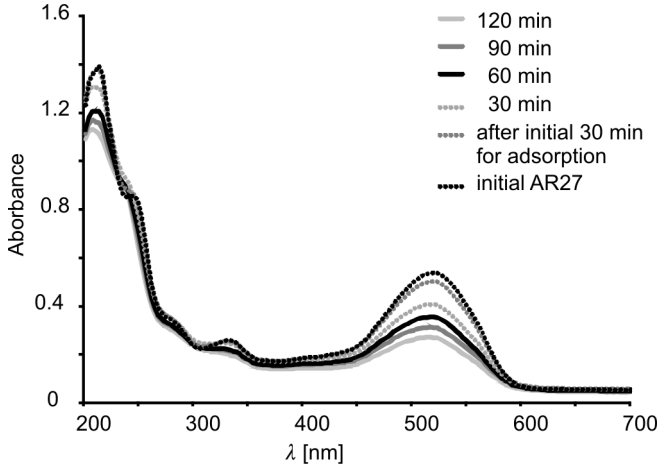


Fig. 8. UV-Vis spectra of $[AR27]_0$= 60 ppm in aqueous $SnO_2$ colloids $[SP-1]_{SnO2}$ = 20 ppm after various irradiation periods

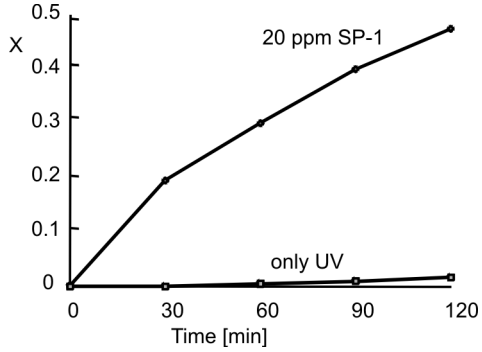


Fig. 9. Effect of irradiation with UV light and $SnO_2$ nanoparticles of $[SP-1]_{SnO_2}$ = 20 ppm on the photocatalytic decolouration of $[AR27]_0$= 60 ppm

The spectra indicate that the intensities of the spectral peaks depend on the irradiation time. The concentration of AR27 in the solution is lower if no irradiation is applied, even if an initial period of 30 min is given for absorbance of the azo dye layer

on the surface of the $SnO_2$ particles. If this step was omitted, the photocatalytic efficiency would be decreased due to insufficient interaction of the dye with the active sites on the surface of the nanoparticles. The change in the dye concentration versus time profile during the photocatalytic decolouration of AR27 with SP-1 nanoparticles is shown in Fig. 9.

The removal of AR27 under irradiation without using any photocatalysts was negligible. The procedure steps of decolouration are as follows [33–36]:

$$SnO_2 + h\nu \longrightarrow SnO_2 \text{ excited (pair electron–hole)} \quad (8)$$

$$h_{VB}^{+} + H_2O \longrightarrow H^{+} + OH^{\bullet} \quad (9)$$

$$h_{VB}^{+} + OH^{-} \longrightarrow OH^{\bullet} \quad (10)$$

$$e_{CB}^{-} + O_2 \longrightarrow O^{2-\bullet} \quad (11)$$

$$O^{2-\bullet} + \text{dye} \longrightarrow \text{dye–OO}^{\bullet} \quad (12)$$

$$O^{2-\bullet} + 2OH^{\bullet} + H^{+} \longrightarrow H_2O_2 + O_2 \quad (13)$$

$$H_2O_2 + h\nu \longrightarrow 2OH^{\bullet} \quad (14)$$

$$OH^{\bullet} + \text{dye} \longrightarrow \text{decolouration of the dye} \quad (15)$$

$$h_{VB}^{+} + \text{dye} \longrightarrow \text{oxidation of the dye} \quad (16)$$

### 3.3. Development of the neural network model

To obtain the optimal network, we tested 132 various neural network architectures with different activation functions and different number of neurons. The data was divided into regions; for each region, training input and test input were selected. This was done continuously, beginning with big regions and reaching smallest possible one. For testing accuracy, the obtained experimental data were plotted versus ANN data in Fig. 10.

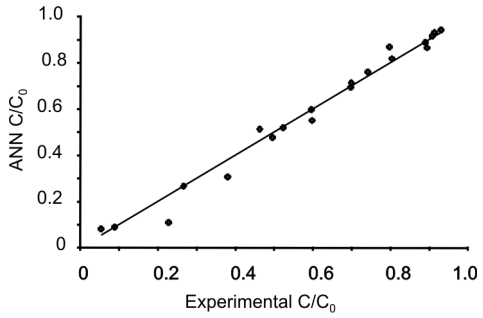


Fig. 10. Calculated and experimental values of the output

Experimental results are in good agreement with a root mean square errors (RMSE) of 0.04053. If the experimental and ANN data have the same values, the bi-

sector line which is shown in Fig. 10 will be carried out. These results confirm that the neural network model could accurately predict the results.

Table 3. Matrix of weights; W1: weights between input and hidden layers; W2: weights between hidden layers and output layers

| W1 | | | | W2 |
|---|---|---|---|---|
| Neuron | Variables | | Bias | Weight |
| | Time | $[AR27]_0$ | | |
| 1 | –12.177 | 11.2939 | 15.2658 | –0.62608 |
| 2 | 4.0292 | –22.6975 | –14.5133 | –0.07613 |
| 3 | 6.6108 | 17.036 | –13.1714 | –0.77583 |
| 4 | 8.2375 | –12.972 | –12.1513 | –0.03141 |
| 5 | –28.0891 | –6.5282 | 10.8794 | –0.1265 |
| 6 | 15.4685 | –1.9166 | –10.2164 | –0.55046 |
| 7 | –3.3571 | 2.8618 | –8.9042 | 1.1693 |
| 8 | 2.5164 | 1.9812 | 7.9623 | –0.02208 |
| 9 | 11.3862 | –14.7485 | –7.0389 | 0.60311 |
| 10 | –16.8626 | –0.61672 | 5.7468 | 0.12029 |
| 11 | –13.3589 | –8.4081 | 4.7322 | –1.0515 |
| 12 | 16.5848 | 9.1167 | –3.7837 | –0.12174 |
| 13 | 10.8791 | 8.8175 | –2.5057 | –0.35808 |
| 14 | 12.7837 | 8.2848 | –1.5429 | 0.77107 |
| 15 | 9.054 | –9.1145 | –0.40496 | 0.022744 |
| 16 | –17.1134 | 5.5002 | –0.55457 | 0.522 |
| 17 | 15.6028 | 2.4898 | 1.3464 | 0.83982 |
| 18 | 11.455 | –13.1046 | 2.5528 | –0.06878 |
| 19 | 2.7418 | –11.1861 | 3.6116 | –0.22561 |
| 20 | 19.567 | 2.5307 | 4.5889 | –0.15973 |
| 21 | 7.7435 | 10.0099 | 5.0492 | –0.28686 |
| 22 | –7.6892 | –13.1195 | –7.2321 | 1.5975 |
| 23 | 11.4763 | 10.1527 | 8.0373 | –0.2725 |
| 24 | –13.0984 | –9.4735 | –8.9793 | –0.12483 |
| 25 | 10.7286 | 14.0612 | 9.9007 | –0.97063 |
| 26 | –11.6994 | –8.8096 | –11.298 | –0.36194 |
| 27 | –15.5001 | 2.3851 | –12.3374 | –0.10918 |
| 28 | –12.3388 | 7.7683 | –13.2593 | –0.02288 |
| 29 | –11.1478 | 10.7477 | –14.3433 | 0.77464 |
| 30 | 7.5182 | 12.9188 | 15.2121 | –0.07348 |

A neural network with thirty neurons in the hidden layer was used with 800 iterations, providing the weights listed in Table 3. The weights are the coefficients between artificial neurons being analogous to synapse strengths between the axons and dendrites in real biological neurons. Therefore, each weight decides what proportion of the incoming signal will be transmitted into the neuron body. In the neural network, the connection weights between neurons are the links between the inputs and the out-

puts, and therefore are the links between the problem and the solution. The relative contributions of the independent variables to the predictive output of the neural network depend primarily on the magnitude and direction of the connection weights. Input variables with larger connection weights represent greater intensities of signal transfer, and therefore are more important in the prediction process compared to variables with smaller weights. Negative connection weights represent inhibitory effects on neurons (reducing the intensity of the incoming signal) and decrease the value of the predicted response, whereas positive connection weights represent excitatory effects on neurons (increasing the intensity of the incoming signal) and increase the value of the predicted response [37].

Garson [38] proposed a method for partitioning the neural network connection weights in order to determine the relative importance of each input variable in the network. It is important to note that his algorithm uses the absolute values of the connection weights when calculating variable contributions, and therefore is insensitive to the direction of changes between the input and output variables. The Garson equation is based on partitioning the weights

$$I_j = \frac{\sum_{m=1}^{m=N_h}\left(\frac{\left|W_{jm}^{ih}\right|}{\sum_{k=1}^{N_i}\left|W_{km}^{ih}\right|}\left|W_{mn}^{ho}\right|\right)}{\sum_{k=1}^{k=N_i}\left(\sum_{m=1}^{m=N_h}\left(\frac{\left|W_{km}^{ih}\right|}{\sum_{k=1}^{N_i}\left|W_{km}^{ih}\right|}\left|W_{mn}^{ho}\right|\right)\right)} \tag{17}$$

where $I_j$ is the relative importance of the $j$th input variable on the output variable, $N_i$ and $N_h$ are the numbers of input and hidden neurons, respectively, the ($W$)s are the connection weights, the subscripts $i$, $h$ and $o$ refer to input, hidden and output layers, respectively, and subscripts $k$, $m$ and $n$ refer to input, hidden and output neurons, respectively, and in this particular case $n = 1$, because there is only one output neuron in the neural network used here.

Table 4. Relative importance of input variables

| Input variables | Importance [%] |
|---|---|
| Initial AR27 concentration | 43.8 |
| Irradiation time | 56.2 |
| Total | 100 |

The relative importance of the variables based on this equation is listed in Table 4. The obtained data using normal inputs between 0 and 1 for training ANN show the

influence of the variables on the decolouration process in which the radiation time is the most influential parameter.

### 3.4. Kinetics of AR27 photocatalytic decolouration

Once the performance of the network was tested, a set of ANN results were obtained from the corresponding variables of AR27 initial concentration and time. Figure 11 shows the output of the ANN as a surface, which enables understanding of the kinetic behaviour of the system.

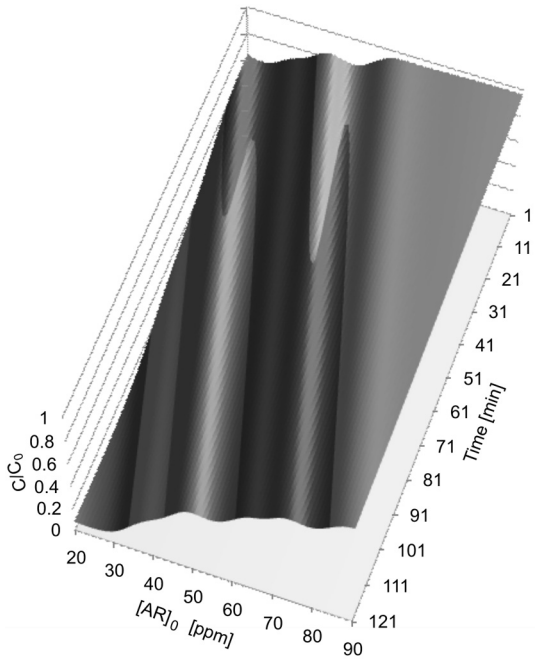


Fig. 11. ANN simulation: effects of the initial pollutant concentration and irradiation time on the decolouration of AR27

It can be easily seen that as has been reported, this pollutant has pseudo-first-order kinetics with respect to the azo dye concentration. Its kinetic profile can be described by:

$$-\ln\frac{[\mathrm{AR27}]}{[\mathrm{AR27}]_0} = k_{\mathrm{obs}}t \tag{18}$$

where $k_{\mathrm{obs}}$ is the pseudo-first-order constant. By applying the least square regression analysis, the values of $k_{\mathrm{obs}}$ were obtained.

From Figure 12, which is same as Fig. 11 but from other point of view, it is evident that at various initial concentrations of AR27, due to changing the concentration of active organic azo dyes in the vicinity of the photocatalysts and at constant rate of

electron-hole creation on its surface, it is possible to change $k_{obs}$ [39]. By increasing the AR27 concentration $k_{obs}$ decreases.

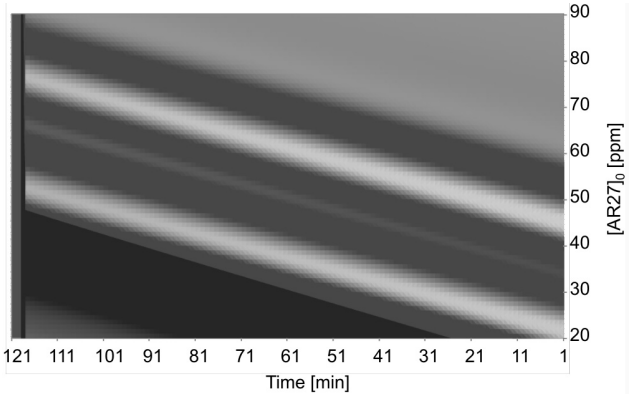


Fig. 12. Irradiation time versus AR27 initial concentration with contour plot of $C/C_0$

The pseudo-first-order kinetics of the decolouration process of azo dye under UV irradiation in the presence of a photocatalyst can be related to the surface adsorption without saturation of active sites. By assuming the Langmuir–Hinshelwood kinetic model, the decolouration reaction rate of AR27 should be proportional to the surface coverage of photocatalytic particles by an organic substance

$$k_c \frac{K_{\mathrm{AR27}}}{1+K_{\mathrm{AR27}}[\mathrm{AR27}]_0} = k_{\mathrm{obs}} \tag{19}$$

$$\frac{1}{k_{\mathrm{obs}}} = \frac{1}{k_c K_{\mathrm{AR27}}} + \frac{[\mathrm{AR27}]_0}{k_c} \tag{20}$$

where $K_{\mathrm{AR27}}$ is the adsorption equilibrium constant, $k_c$ is the kinetic rate constant of surface reaction and $[\mathrm{AR27}]_0$ is the initial concentration of AR27 [40].

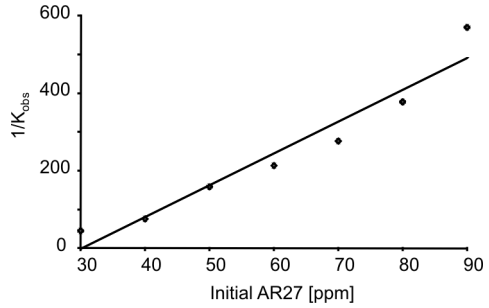


Fig. 13. Dependence of $K_{obs}$ (1/min) calculated from ANN on the initial concentration of AR27

Figure 13 shows the dependence of $1/k_{obs}$ on initial concentration of AR27, from the ANN data. In the Langmuir–Hinshelwood equation, $k_c$ is related to the limiting

rate of the reaction at the maximum coverage under the experimental conditions and $K_{AR27}$ represents the equilibrium constant for adsorption of AR27 on the surface of an active photocatalysts [40]. By means of a least square best fitting procedure, the values of the adsorption equilibrium constant $K_{AR27}$ and the kinetic rate constant of surface reaction $k_c$ were calculated to be 0.0331 $dm^3$/mg and 0.1218 mg/(min·$dm^3$), respectively.

## 4. Conclusions

The synthesis of $SnO_2$ nanoparticles with relatively high specific surface area and small crystallite sizes has been reported. The synthesized nano-$SnO_2$ exhibited mesoporous-like behaviour. The statistical film thicknesses of materials adsorbed were used for estimating pore sizes which showed a decrease with increase in hydrothermal period. In addition, the photocatalytic decolouration efficiency of these particles for decolouration of AR27 has been investigated. Results indicated that the decolouration rate and efficiency were highly affected by the initial AR27 concentration and the specific surface area of the photocatalyst. The photocatalytic decolouration of AR27 can be explained in terms of the Langmuir–Hinshelwood kinetic model. The results obtained from this model are in good agreement with the experimental data. The mechanism of the photochemical decolouration of Acid Red 27 solution by using $SnO_2$ nanopowders was successfully predicted by applying a three-layered neural network with thirty neurons in the hidden layer, and using a back-propagation algorithm. Simulations based on the ANN model were performed in order to estimate the behaviour of the system under various conditions. The parameters investigated in this work (i.e., initial concentration of the dye and reaction time) have considerable influence on the decolouration efficiency and, as expected, the irradiation time with a relative importance of 56.2%, appeared to be the more influential factor. The results of data modelling confirmed that neural network modelling could effectively predict the behaviour of the system.

### References

[1] KONSTANTINOU I.K., ALBANIS T.A., Appl. Catal. B. Environ., 49 (2004), 1.
[2] STOLZ A., Appl. Microbiol. Biotechnol., 56 (2001), 69.
[3] O'NEILL C., HAWKES F.R., HAWKES D.L., LOURENCO N.D., PINHEIRO H.M., DELÉE W., J. Chem. Tech. Biotechnol., 74 (1999), 1009.
[4] ROBINSON T., MCMULLAN G., MARCHANT R., NIGAM P., Bioresource Technol., 77 (2001), 247.
[5] BAHNEMANN D., CUNNINGHAM J., FOX M.A., PELIZZETTI E., PICHAT P., SERPONE N., *Photocatalytic Treatment of Waters in Aquatic and Surface Photochemistry*, Lewis Publishers, Boca Raton, 1994.
[6] VALSARAJ K.T., RAVIKRISHNA R., LIN H., YUAN Q., Proc. Symp. ICMAT 2001: *Advances in Environmental Materials, Vol. I. Pollution Control Measures*, Materials Research Society (Singapore), Singapore, 2001.
[7] SAFARIK I., NYMBURSKA K., SAFAIKOVA M., J. Chem. Tech. Biotechnol., 69 (1997), 1.

[8] KUO W.G., Wat. Res., 26 (1992), 881.
[9] MORISSON C., BANDARA J., KIWI J., LOPEZ A., J. Adv. Oxid. Technol., 1 (1996), 160.
[10] SILVA C.G., WANG W., FARIA J.L., J. Photochem. Photobiol. A: Chem., 181 (2006), 314.
[11] STYLIDI M., KONDARIDES D.I., VERYKIOS X.E., Appl. Catal. B: Environ., 47 (2004), 189.
[12] HERRMANN J.M., Catal. Today, 53 (1999), 115.
[13] XI L., QIAN D., TANG X., CHEN C., Mater. Chem. Phys., 108 (2008), 232.
[14] WANG H.C., LI Y., YANG M.J., Sensor. Actuat. B: Chem., 119 (2006), 380.
[15] NAYRAL C., VIALA E., COLLIÈRE V., FAU P., SENOCQ F., MAISONNAT A., CHAUDRET B., Appl. Surf. Sci., 164 (2000), 219.
[16] MUKHOPADHYAY A.K., MITRA P., CHATTERJEE A.P., MAITI H.S., Ceram. Int., 26 (2000), 123.
[17] TEERAMONGKONRASMEE A., SRIYUDTHSAK M., Sens. Actuators, B, Chem., 66 (2000), 256.
[18] EMILIO C.A., MAGALLANES J.F., LITTER M.I., Anal. Chim. Acta, 595 (2007), 89.
[19] DURAN A., MONTEAGUDO J.M., Water Res., 41 (2007), 690.
[20] TOMA F.L., GUESSASMA S., KLEIN D., MONTAVON G., BERTRAND G., CODDET C., J. Photochem. Photobiol. A: Chem., 165 (2004), 91.
[21] MORGAN D.P., SCOFIELD C.L., *Neural Networks and Speech Processing*, Kluwer, London, 1991.
[22] CULITY B.D., Elements of X-ray diffraction, 2nd Edition, Addison-Wesley Company, USA, 1978.
[23] DUONG D.D., *Adsorption Analysis: Equilibria and Kinetic*s, Imperial College Press, Australia, 1998.
[24] GREGG S.J., SING K.S.W., *Adsorption, Surface Area and Porosity*, 2nd Ed., Academic pRess, London, 1982.
[25] HALSEY J., J. Chem. Phys., 16 (1948), 931.
[26] YANG M., WANG G., YANG Z., Mater. Chem. Phys., 111 (2008), 5.
[27] MOHAMMADI M.R., FRAY D.J., MOHAMMADI A., Micropor. Mesopor. Mater., 112 (2008), 392.
[28] CHUNG K.H., CHANG D.R., PARK B.G., Bioresource Tech., 99 (2008), 7438.
[29] WEN Z., WANG Q., ZHANG Q., LI J., Adv. Funct. Mater., 17 (2007), 2772.
[30] ZHONG W.Z., LIU G.Z., Sci. China (B), 24 (1994), 394.
[31] LI W.J., SHI E.W., ZHONG W.Z., YIN Z.W., J. Cryst. Growth, 203 (1999), 186.
[32] WANG W.W., Mater. Res. Bull., 43 (2008), 2055.
[33] BEHNAJADY M.A., MODIRSHAHLA N., HAMZAVI R., J. Hazard. Mater. B, 133 (2006), 226.
[34] KHODJA A.A., SEHILI T., PILICHOWSKI J., BOULE P., J. Photochem. Photobiol. A: Chem., 141 (2001), 231.
[35] DANESHVAR N., SALARI D., KHATAEE A.R., J. Photochem. Photobiol. A: Chem., 162 (2004), 317.
[36] HOFFMANN M.R., MARTIN S.T., CHOI W., BAHNEMANN D., Chem. Rev., 95 (1995), 69.
[37] SLOKAR Y.M., ZUPAN J., MARECHAL A.M.L., Dyes Pigments, 42 (1999), 123.
[38] GARSON G.D., AI Expert, 6 (1991), 47.
[39] MILLS A., DAVIS R.H., WORSELY D., Chem. Soc. Rev., 22 (1993), 417.
[40] OLLIS D.F., Top. Catal., 35 (2005), 217.

*Received 29 July 2008*
*Revised 17 June 2009*